Energy Advances

Accepted Manuscript

This article can be cited before page numbers have been issued, to do this please use: D. Xi, Z. Yang, A. M. Alfaraidi, Y. Jing, R. G. Gordon and M. J. Aziz, *Energy Adv.*, 2024, DOI: 10.1039/D4YA00279B.

ROYAL SOCIETY OF CHEMISTRY

rsc.li/energy-advances

View Article Online
DOI: 10.1039/D4YA00279B

Single-membrane pH-decoupling Aqueous Batteries Using Proton-coupled Electrochemistry for pH Recovery

Dawei Xi[1], Zheng Yang[1], Abdulrahman M. Alfaraidi[1], Yan Jing[2], Roy G. Gordon[1,2], Michael J. Aziz[1,*]

1 John A. Paulson School of Engineering and Applied Sciences, Harvard University, Cambridge, MA, USA.

2 Department of Chemistry and Chemical Biology, Harvard University, Cambridge, MA, USA

* E-mail: maziz@harvard.edu

Data availability

The datasets analyzed and generated during the current study are included in the paper, its Supplementary Information and uploaded to Figshare at https://doi.org/10.6084/m9.figshare.25962982

View Article Online
DOI: 10.1039/D4YA00279B

Single-membrane pH-decoupling Aqueous Batteries Using Proton-coupled Electrochemistry for pH Recovery

Dawei Xi[1], Zheng Yang[1], Abdulrahman M. Alfaraidi[1], Yan Jing[2], Roy G. Gordon[1,2], Michael J. Aziz[1,*]

1 John A. Paulson School of Engineering and Applied Sciences, Harvard University, Cambridge, MA, USA.

2 Department of Chemistry and Chemical Biology, Harvard University, Cambridge, MA, USA

* E-mail: maziz@harvard.edu

TOC: Proton-coupled electrochemical reactions as proton pumps can facilitate in-situ or ex-situ pH recovery and capacity rebalancing within single-membrane pH-decoupling batteries.

Abstract:

pH-decoupling in aqueous redox flow batteries (ARFBs) represents a promising strategy for enhancing cell voltage and expanding the repertoire of redox pair combinations. Effective management of acid-base crossover and the implementation of cost-effective pH recovery methods are pivotal for long-term stability of pH-decoupling ARFBs. We introduce a pH-decoupling design integrated into a conventional single-membrane ARFB architecture. This approach reduces the area specific resistance while suppressing acid-base crossover to an acceptable level. We explore various electrolyte pairs, ranging from anions to cations, acids to bases, always dissolved to electrodepositing, showing the flexibility afforded by this design in selecting electrolyte compositions. Furthermore, we demonstrate the utility of proton-coupled electrochemical reactions as proton pumps, facilitating *in-situ* or *ex-situ* pH recovery within pH-decoupling batteries. Our findings potentially offer benefits including improved energy efficiency, increased areal power output, and decreased capital costs, thereby advancing the prospects for scalable and sustainable energy storage solutions.

Broader context:

Aqueous redox flow batteries (ARFBs) stand out as a leading solution for economical and scalable storage of intermittent renewable energy derived from sources like wind and solar. For long time storage (> 8 h), these batteries offer a unique advantage by decoupling energy storage from power generation, providing a level of design versatility and scalability that traditional rechargeable batteries can hardly match. Traditionally, ARFBs maintain a uniform pH in both negolyte and posolyte to ensure consistent and stable operation over the long term. However, introducing disparate pH levels within a single cell, especially using acid for posolyte and base for negolyte, would broaden the choice of high voltage candidate redox couples. This approach also facilitates the pairing of redox couples that necessitate distinct pH environments, thereby enhancing the versatility and efficacy of the system. Our research demonstrated that different pH can be used in a conventional ARFB architecture, while the acid-base crossover is not a fatal drawback. We also showed that proton-coupled electrochemistry can be used to maintain the pH difference across the cell, paving the way toward the commercialization of pH-decoupling batteries.

Driven by decarbonization, the rapid expansion of renewable energy sources like wind and solar incentivizes the development of robust energy storage systems to regulate their fluctuating power output.[1]

View Article Online
DOI: 10.1039/D4YA00279B

Aqueous redox flow batteries (ARFBs) emerge as a viable option, offering safety, long discharge duration at rated power, and the potential for both longevity and affordability.[2] Through the transition from solid electrodes to liquid flowable electrolytes, ARFBs facilitate the independent optimization of energy capacity and power output, thereby augmenting system design versatility.[3] Advancements in redox-active materials are also bringing us closer to realizing the practical feasibility of grid-scale storage.[4-8]

In the conventional design of ARFBs, a single ion exchange membrane is utilized to separate the negolyte and posolyte.[9] For example, an anion-exchange membrane (AEM) can block cationic redox-active species, serving to prevent self-discharge while simultaneously allowing the migration of non-reactive anions to maintain charge balance in the electrolytes. Likewise, a cation-exchange membrane (CEM) is effective for cells that use anionic redox-active species. In most cases, maintaining the same time-averaged value of the pH on both sides the cell is pursued to suppress proton or hydroxide crossover.[8]

A higher voltage can increase the practicability of ARFBs by raising energy and power density, thereby lowering capital costs.[10] The emerging strategy of pH-decoupling ARFBs, employing negolytes and posolytes with distinct pH values, is drawing attention, due to its potential to achieve higher voltages.[11] Tailored ion-selective and bipolar membranes have been used in the development of single-membrane pH-decoupling ARFBs. [12-14] Moreover, the use of multi-membrane cell architectures has enabled higher flexibility in the selection of negolyte and posolyte active species.[15-17] However, pH-decoupling systems are susceptible to proton/hydroxide crossover caused by the pH difference, which compromises longevity and overall efficiency.[18] Recently, the acid/base crossover rate in pH-decoupling systems was systematically studied and *ex-situ* pH recovery using bipolar membrane sub-cells was realized, making the pH-decoupling system practical for efficient, long-term operation.[19]

Unfortunately, most pH-decoupling systems have high area specific resistance, which dramatically lowers the benefits derived from pH-decoupling. Also, the multi-chamber multi-membrane cell architecture or the utilization of a bipolar membrane increases the capital cost and the operational complexity. Herein, we report the decoupling of the pH of the posolyte and negolyte in a single-membrane ARFB of conventional architecture and the investigation of its performance. By employing a variety of redox couples, we studied the cycling patterns and power generation potential inherent in this design, utilizing either an AEM or a CEM. Additionally, we estimated the crossover rate of acid and base, which is a vital factor for ensuring the sustained operation of pH-decoupled flow systems over extended periods. To recover the crossover of acid and base, we utilized a proton pump that runs proton-coupled electron transfer (PCET) reactions inside or outside the original cell. The proton pump can use water splitting, the oxygen reduction reaction (ORR) or the hydrogen oxidation reaction (HOR) as side-reactions to recover the pH, provided that the reductive and oxidative side-reactions are balanced. With such a design and suitable proton pumps, different types of electrolytes – even electrodepositing batteries (aqueous batteries involving electrodeposition on one or both sides)[20, 21] – can potentially leverage a pH-decoupling architecture to exhibit stable operation at higher voltage.

Decoupling the pH in a single membrane conventional ARFB architecture has been reported,[22-25] yet the long-term acid-base crossover in the cell has not been considered. An AEM type single-membrane pH-decoupling ARFB with cationic redox-active candidates is illustrated in **Fig. 1a**. To maintain non-hydroxide anions as main charge carriers, the hydroxide concentration in the negolyte must remain dilute. Yet for a highly selective AEM, the cell is workable with an acidic posolyte of low pH. Acid-base crossover is caused by proton crossover and hydroxide exchange through the AEM. Similarly, the posolyte in a CEM type pH-decoupled ARFB with anionic redox-active species requires a dilute proton/hydronium concentration (**Fig. 1b**), but the cell is workable with a high-pH negolyte. The fluxes for acid-base crossover are depicted at the bottom of the diagram and described in **Supplementary Note. 1**. The influence of acid-base crossover is

View Article Online
DOI: 10.1039/D4YA00279B

decoupled from the electrolyte volume (total capacity). Researchers can find suitable conditions for specific redox active molecules if acid-base crossover remains sufficiently low to avoid significant impacts on energy efficiency and acid-base regeneration is provided. Detailed structures and properties of listed redox molecules are in **Supplementary Table. S1**.

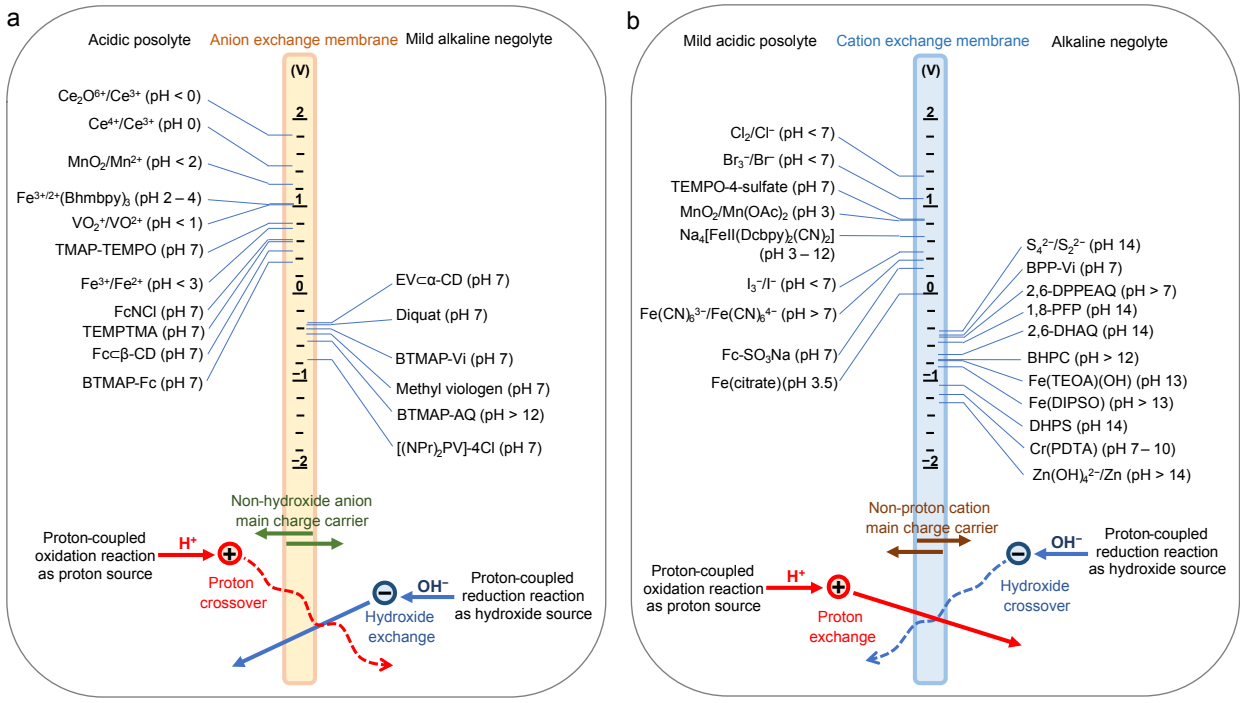

Figure 1 | Single-membrane pH-decoupling ARFBs. Schematic of **a,** an AEM type and **b,** a CEM type single-membrane pH-decoupling ARFB with potential redox candidates with voltage vs. standard hydrogen electrode (SHE) identified. Main charge carriers and possible acid-base crossover processes are labeled at the bottom.

To demonstrate these principles, we paired 5 mL of 0.1 M tris(4,4'-bis(hydroxymethyl)-2,2'-bipyridine) iron dichloride ($Fe(Bhmbpy)_3$) as capacity limiting side with 10 mL 0.1 M 1,4-bis[3-(trimethylammonio)propyl]-anthraquinone (BTMAPAQ) in an AEM type pH-decoupling ARFB (**Fig. 2a**).[26, 27] The redox potential of $Fe(Bhmbpy)_3$ is about 0.98 V vs. SHE, and the potential of BTMAPAQ at pH 12 is about −0.55 V vs. SHE. The posolyte was buffered by the ligand, operating within a pH range of approximately 2 – 4. The redox reaction of BTMAPAQ is proton-coupled when the electrolyte pH is below 12, transitioning to a non-proton-coupled reaction at higher pH. Thus, we set the initial pH of the BTMAPAQ at 12. To separate the cell, we employed Selemion DSV-N as the AEM. All cell characterization procedures were conducted within a nitrogen glovebox. We used standard constant-current followed by constant-voltage (CCCV) protocol at 40 mA cm^{-2} with voltage cut-off values of 1.75 V and 0.4 V, held until the current density dropped below 5 mA cm^{-2} and 1 mA cm^{-2} during charge and discharge, respectively. Analysis revealed the acid crossover flux to be lower than 1 nmol s^{-1} cm^{-2} (0.1 mA cm^{-2}), with the base exhibiting an approximate flux of 4 nmol s^{-1} cm^{-2} (Supplementary note. S1). The cell capacity, Coulombic efficiency and pH of posolyte and negolyte during cell cycling are shown in **Fig. 2b** and **2c**. The cell accessed >90% of its theoretical capacity and exhibited an average Coulombic efficiency of 98.5%,

View Article Online
DOI: 10.1039/D4YA00279B

with $Fe(Bhmbpy)_3$ as the capacity limiting side. Because of the side-reaction of ligand oxidation in the posolyte,[26] the Coulombic efficiency of the system is limited by the posolyte side, leading to a drift from initial charge balance toward reduction of both sides. To offset this imbalance during cell cycling, we introduced oxygen into BTMAPAQ when the cell was nearly discharged and the pH of negolyte became low or the cell was out of balance. Each time the negolyte was exposed to oxygen, the cell went back into balance and the pH difference between posolyte and negolyte increased.

The reactions contributing to the recovery of pH are listed in **Fig. 2d**. These side reactions do not contribute to capacity, but they cause Coulombic efficiency loss. Introducing oxygen into the negolyte containing reduced anthraquinones leads to the oxidation of anthraquinones, generating hydroxide or peroxide.[28] The net reactions are the ORR through 2e or 4e pathways.[29] During the oxygen exposure periods, the posolyte pH also slightly decreased; the proton source might be the oxidation of peroxide anions generated in the negolyte and crossing the AEM (**Supplementary Fig. S1**). Additionally, despite being an undesirable side reaction and contributing to the fading observed in Fig. 2b, the oxidation of ligands can act as a proton source (**Supplementary Note. 2**). With future development of a more stable ligand, applying a high positive voltage to the posolyte to drive the oxygen evolution reaction (OER) can possibly be an ideal proton source. By operating the cell outside of the glovebox, aside from the main redox reactions, when all the oxidation reactions happening in the posolyte balanced all the reduction reactions in the negolyte, states of charge (SOC) of both sides of the cell remained balanced (**Fig. 2e**). Because these minor reactions are all proton-coupled electrochemistry, acting as proton pumps, a relatively stable pH was maintained (**Fig. 2f**).

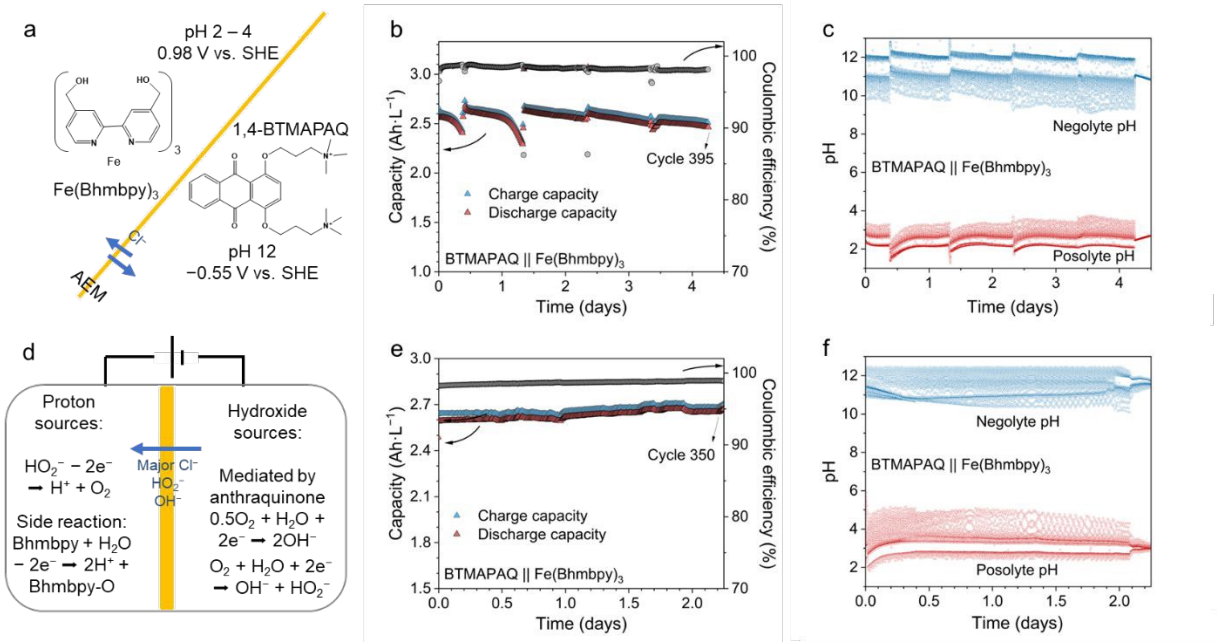

Figure 2 | Operation of an AEM pH-decoupling ARFB. a, Chemistry and properties of the cell. **b,** Discharge capacity, charge capacity and Coulombic efficiency of the cell during CCCV cycling under nitrogen. Cell can run out of balance due to the self-discharging of the posolyte. Oxygen was introduced into the cell about day 0.5, 1.5, 2.5 and 3.5 to restore the balance of the posolyte and negolyte. **c,** pH of the cell during CCCV cycling showed in b. The pH difference of the posolyte and the negolyte increased after oxygen was introduced. **d,** Proton-coupled side reactions in the cell that do not contribute to the cell capacity but can maintain the pH difference. **e,** Discharge capacity, charge capacity and Coulombic efficiency of the cell during CCCV cycling in air. **f,**

View Article Online
DOI: 10.1039/D4YA00279B

Negolyte pH and posolyte pH of the cell during CCCV cycling showed in e. BTMAPAQ constantly reacted with oxygen in the air, without showing obvious pH fluctuations.

We then conducted a galvanostatic and polarization analysis of the cell. During galvanostatic tests, the potential was held at the end of discharge in order to recover $Fe(Bhmbpy)_3$ from dimerization (**Supplementary Fig. S2**).[26] When the current density was increased from 40 to 80 mA cm^{-2}, the Coulombic efficiency of the cell maintained about 98%. Capacity utilization of the cell dropped from 90% to 65%, accompanied by a reduction in round-trip energy efficiency from 68% to 40% (**Supplementary Fig. S3**). Polarization curves and galvanic power densities are shown in **Supplementary Fig. S4**. The cell reached a peak power density of 140 mW cm^{-2} at 80% SOC. **Supplementary Fig. S5** shows the OCV of the cell is about 1.5 V. The high-frequency area-specific resistance (ASR) of the battery averaged 1.45 Ω cm^2 while the average polarization ASR across all SOCs was 2.9 Ω cm^2. These values indicate that the ohmic resistance of the cell is low, owing to the single membrane setup, but the charge transfer resistance of the redox molecules, possibly augmented with a mass transport overpotential, also contributed 50% to cell's overall resistance.

In a demonstration of a pH-decoupling ARFB with a CEM design, bromide/bromine was utilized in the posolyte and an anionic anthraquinone was utilized in the negolyte. We chose (((9,10-dioxo-9,10-dihydroanthracene-2,6-diyl)bis(oxy))bis(propane-3,1-diyl))bis(phosphonic acid) (2,6-DPPEAQ) for the negolyte due to its high solubility at pH ≳ 9.[30] The initial pH was set to 12 for 0.25 M DPPEAQ. Poly acrylic acid (PAA, MW = 2000) was added to 1 M NaBr in the posolyte to stabilize the posolyte pH at approximately 4. Nafion 212 was used as the CEM without pre-treatment. Galvanostatic tests of the cell with a cutoff voltage of 2 V and 0.7 V are shown in **Fig. 3a**. During galvanostatic tests, the Coulombic efficiency of the cell maintained about 95% to 98%. Capacity utilization of the cell dropped from 92% to 65%, and the round-trip energy efficiency dropped from 77% to 55% as the current density was increased from 20 to 80 mA cm^{-2} (**Supplementary Fig. S6**). From polarization tests, the OCV of the cell was approximately 1.6 V, with a high frequency ASR of 1.6 Ω cm^2 and a polarization ASR of 4.6 Ω cm^2 (**Supplementary Fig. S7**). The cell did not exhibit signs of mass transport limitation under 300 mA cm^{-2} during discharge, due to a higher concentration of the redox active molecules than in the $Fe(Bhmbpy)_3$/BTMAPAQ cell. The cell reached a peak power density of 190 mW cm^{-2} at 70% SOC (**Supplementary Fig. S8**). During cell cycling in air, we used a CCCV protocol at 40 mA cm^{-2} with voltage cut-off values of 2.0 V and 0.7 V, held until the current density dropped below 10 mA cm^{-2} and 5 mA cm^{-2} during charge and discharge, respectively. During cell cycling, the charge and discharge capacity (**Fig. 3b**) remained stable, with a Coulombic efficiency about 99%. The pH of the cell was relatively stable, due to low acid/base crossover (estimated as lower than 1 nmol s^{-1} cm^{-2}), and proton-coupled side reactions (**Fig. 3c**). Mediated ORR served as a hydroxide source on the anthraquinone side,[28] while on the bromide side, the oxidation of carbon and PAA buffer by bromine, although unfavorable side reactions, provided protons and maintained cell balance.[31] With the future development of a more stable electrode and buffer chemistry for bromide posolyte in a practical long-term cell cycling, water oxidation can serve as an ideal proton pump to balance hydroxide crossover (**Supplementary Note. 2**).

View Article Online
DOI: 10.1039/D4YA00279B

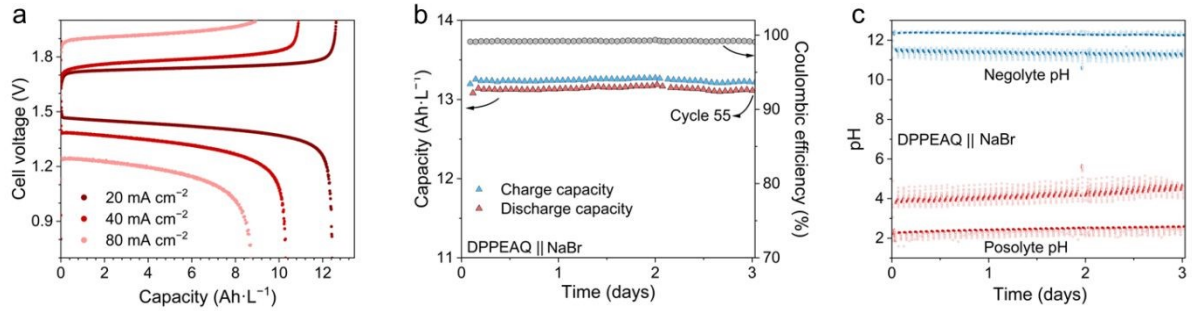

Figure 3 | Operation of a CEM pH-decoupling ARFB. a, Galvanostatic charge-discharge voltage-capacity profile for the DPPEAQ-NaBr cell. Capacity is reported in Ampere-hours per liter of negolyte. **b,** Charge capacity, discharge capacity and Coulombic efficiency of the cell during CCCV cycling under nitrogen. **c,** Negolyte and posolyte pH during CCCV cycling shown in b.

In pH-decoupling ARFBs where both the posolyte and negolyte redox couples are soluble and flowable, a pH-recovery system employing a bipolar membrane (BPM) for water dissociation can be implemented.[19, 32] However, for pH-decoupling electrodepositing batteries in which one state of the redox couple exists in solid form, it becomes challenging to introduce them into a pH-recovery BPM sub-cell for discharge and subsequent water dissociation. Instead, *in-situ* pH recovery can be done inside the main cell. Several pH-decoupling electrodepositing batteries have been reported.[33, 34] For example, alkaline Zn – halogen cells have reported high voltage, high power and high energy density.[20, 24] Alkaline Zn-Br ARFB can exhibit an OCV of 2.3 V. [35] The $Zn(OH)_4^{2-}/Zn$ couple, composing the negolyte, exhibits a low potential of −1.22 V vs. SHE at pH 14, whereas halogen/halide redox couples, being highly positive, necessitate operation at pH levels below 7 to avoid disproportionation. Additionally, MnO_2/Mn^{2+} has also been demonstrated in pH-decoupling cells,[21, 34] showing promising cell cycling and energy efficiency. These works, however, did not address the management of acid-base crossover. Proton-coupled electrochemistry, as demonstrated with proton pumps, could also be employed in such systems to ensure pH stability. As a demonstration, we assembled a pH-decoupling Zn-Mn aqueous battery that uses water splitting to generate acid and base. For the posolyte, we used an acetic acid (HOAc)/sodium acetate (NaOAc) buffer to support $MnO_2/Mn(OAc)_2$, whose redox reaction is mediated by low concentration iodine.[21] For the negolyte, we used $Na_2Zn(OH)_4/Zn$, known for its high voltage and cost-effectiveness but prone to dendrite formation (**Fig. 4a**).[18] 1 M $Mn(OAc)_2$ in 3 M HOAc, with 1 M NaOAc and 0.05 M KI as posolyte, and 1 M $Na_2Zn(OH)_4$ with 2 M NaOH as negolyte were pumped through carbon cloths at a flow rate of 30 mL min^{-1}. In galvanostatic tests, the cell was charged to 10 mAh cm^{-2} at 20 mA cm^{-2} and discharged at various current densities (**Supplementary Fig. S9**). The round-trip energy efficiency dropped from 85% to 70% as the discharging current density was increased from 20 to 60 mA cm^{-2}. The high-frequency ASR of the battery was about 1.7 Ω cm^2 while the polarization ASR was 6.8 Ω cm^2 due to the slow kinetics of the redox couples. Linear sweep voltammetry tests of the charged cell demonstrated an OCV about 1.9 V and a peak power density of 280 mW cm^{-2} (**Fig. 4b**). Crossover of hydroxide was about 10 nmol s^{-1} cm^{-2}, due to the utilization of high concentration of NaOH (> 2 M) for supporting $Na_2Zn(OH)_4$.[19] Such crossover rates can cause cycling instability in the long run by decreasing the pH difference between negolyte and posolyte. This can be mitigated by driving water splitting across the cell. As shown in **Fig. 4c, d**, by applying 3 V during charging for about 1 min while cutting the flow rate to 2 mL min^{-1}, the pH difference between the posolyte and the negolyte increased. While water splitting serves as an ideal proton pump, forced OER and hydrogen evolution reaction (HER) can be problematic. Although they produce protons, unfavored side reactions like

View Article Online
DOI: 10.1039/D4YA00279B

the oxidation of iodine and acetates could also happen. A large voltage applied on the cell also drove fast growth of Zn dendrites on the negolyte side, leading to a faster cell failure. Passive reactions like ORR and HOR might be safer and more controllable proton pumps in some cases. *Ex-situ* HOR can also serve as a proton source for posolytes when suitable. We provided an external source of hydrogen gas to react with posolyte, catalyzed by Pt, to generate protons, as shown in **Supplementary Fig. S10**.

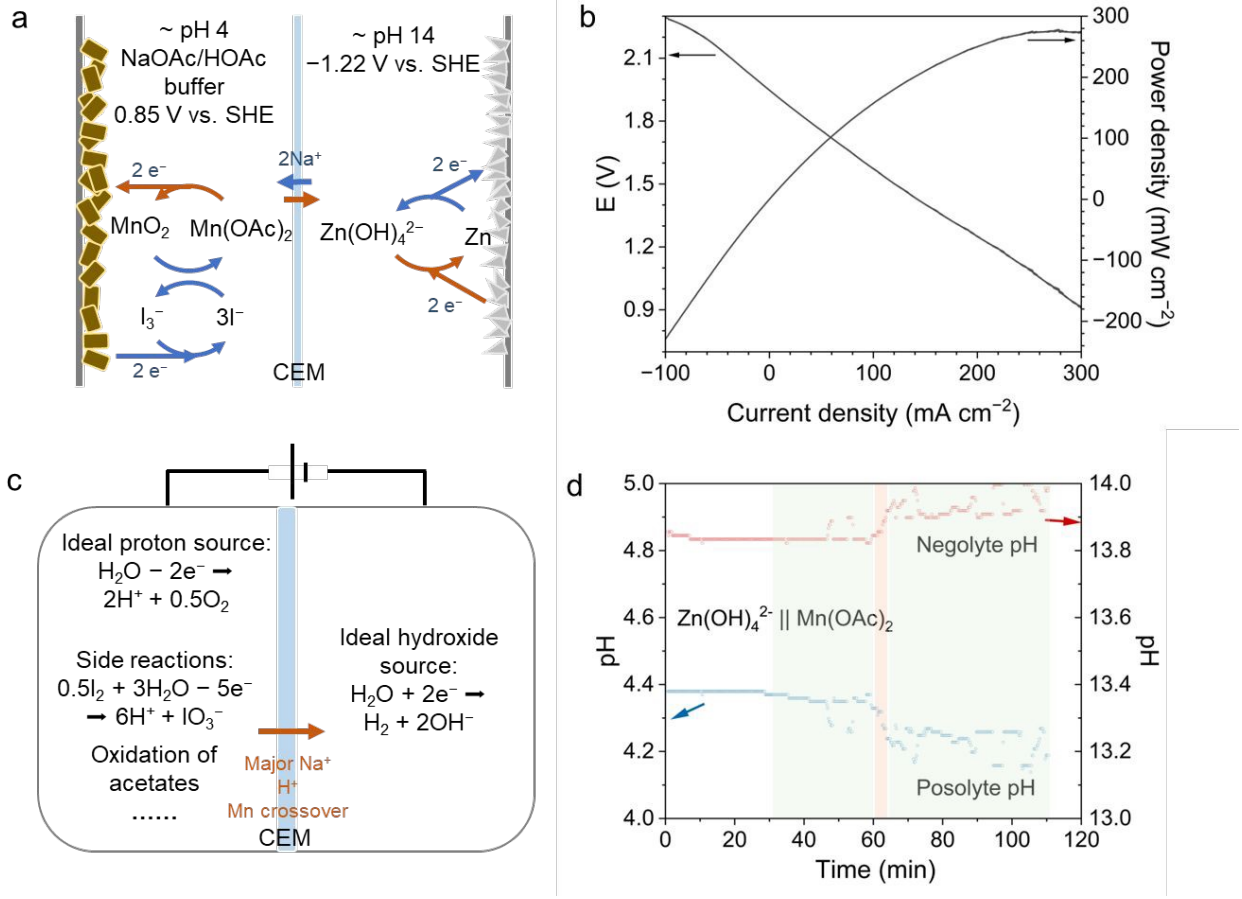

Figure 4 | pH recovery in a pH-decoupling electrodepositing battery. a, Chemistry and properties of the cell. Reactions during charging are marked with red arrows, and reactions during discharging are marked with blue arrows. Iodide was added to accelerate and complete the reduction of MnO_2. $Mn(OAc)_2$, HOAC and other small ions exhibit unwanted crossover through the CEM. **b,** Cell voltage and power density of the cell during discharge. **c,** Reactions during over-charging driven water splitting. **d,** pH of the cell during charging (green shade) and over-charging (red-shade).

Runing proton-coupled electrochemical reactions as proton pumps to balance acid/base crossover can be an *in-situ*, inexpensive and convenient method to maintain operational stability of pH-decoupling ARFBs. However, as demonstrated, the rebalancing reactions need to be carefully chosen to avoid unwanted side reactions .pH-decoupling cells demonstrated in this work all have unwanted side-reactions or operational challenges to some extent. There are ways to suppress side-reactions. For example, employing a sub-cell

View Article Online
DOI: 10.1039/D4YA00279B

with catalysts for reactions that function as proton pumps, or directly integrating catalysts in the main cell, can possibly increase the selectivity of reactions (**Fig. 5a**).[36] Yet the key is to find proton-coupled electrochemistry that matches the redox couples utilized in the cell. As long as the cell remains balanced, self-discharging reactions can be ideal for maintaining pH, involving only water chemistry (2e ORR, 4e ORR, OER, peroxide oxidation, HER, HOR), resulting in the proton pumping rate matching the acid-base crossover rate at steady-state (**Supplementary Table S2**).[28, 31, 37]

Using water dissociation as a proton pump in BPM sub-cells is more compatible with less robust redox couples and is more controllable because it only requires normal discharging and generates acid and base symmetrically.[19] But it can be difficult to use in redox couples involving electrodeposition. To utilize a BPM sub-cell for pH recovery in pH-decoupling electrodeposition batteries, redox molecules of which both redox states are soluble must be added (**Fig. 5b**). For example, in the case of MnO_2/$Mn(OAc)_2$ that uses iodide/iodine as a redox mediator, iodine can serve as a flowable redox couple to be discharged in the BPM cell. Generally, a small concentration of always-soluble redox mediators that have a lower redox potential than that of the posolyte species, but a higher potential than that of the negolyte species, can be deliberately added into electrolytes to realize BPM pH recovery (**Supplementary Note. 3**).

Proton-coupled electrochemistry and water dissociation as proton pumps are interconnected strategies. In instances where the rate of acid-base generation through proton-coupled electrochemistry fails to match the acid-base crossover rate,[3] the utilization of a BPM sub-cell can help stabilize the pH. In some special cases, BPM sub-cells can be used to maintain a uniform pH in ARFBs that have ideally zero acid-base crossover rate but have proton coupled self-discharging reactions. If the cell goes out of balance, however, due to asymmetric self-discharge, the BPM sub-cell cannot rebalance the cell. But if self-discharging reactions are proton-coupled water electrochemistry, e.g. the HER, then proton-coupled water electrochemistry can be applied to one side as a proton pump, balancing the cell capacity and acid-bass loss. For example, one can drive the OER when the cell is over-oxidized due to negolyte self-discharging, or one can drive the ORR when the cell is over-reduced due the posolyte self-discharging. Through coupled generation or neutralization of protons and hydroxide, maintaining the cell balance with proton-coupled electrochemistry helps adjust the pH of posolyte and negolyte symmetrically.

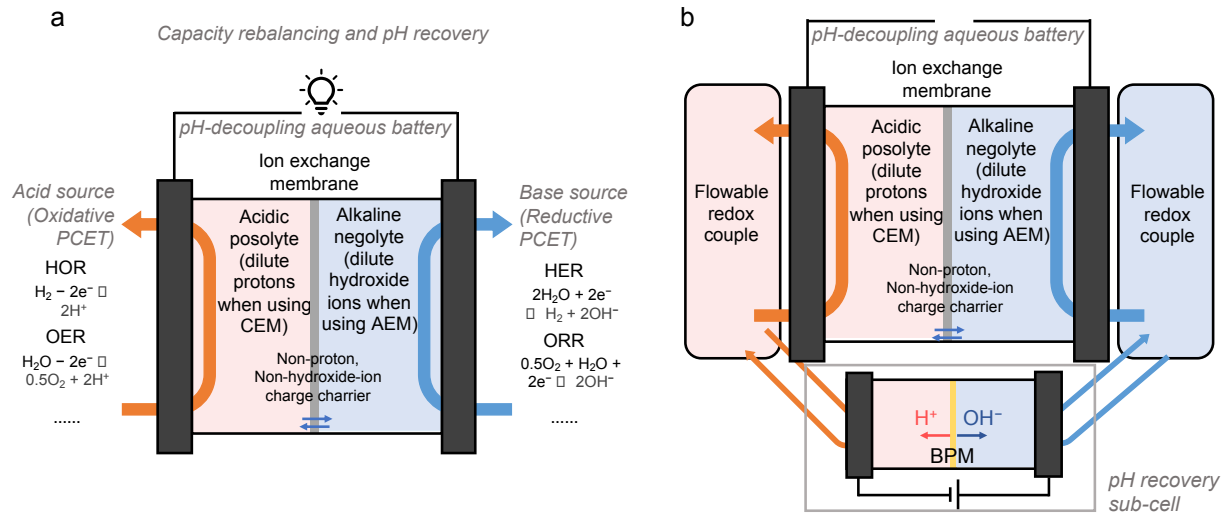

View Article Online
DOI: 10.1039/D4YA00279B

Figure 5 | pH-decoupling ARFBs with different pH recovery strategies. a, A pH-decoupling cell using proton-coupled electrochemistry for capacity rebalancing and pH recovery. The reactions functioning as proton pumps, identified as acid source and base source, may occur in the cell as in-situ pH recovery or outside the cell as ex-situ pH recovery. Catalysts for proton pumps can be introduced to lower the overpotential of these PCET reactions. **b,** A pH-decoupling cell using a BPM sub-cell for pH recovery. The cell must contain flowable redox molecules to drive water dissociation in the BPM cell.

Conclusion

With suitable redox couples, pH-decoupling can be realized in a conventional single membrane cell architecture, exhibiting acceptably low acid-base crossover flux and lower ohmic resistance compared to multi-membrane cells. In CEM pH-decoupling ARFBs, it's possible to employ a high concentration of strong base in the negolyte against a posolyte with a dilute proton concentration. AEM type pH-decoupling ARFBs, if outfitted with a highly selective AEM, can use highly concentrated strong acid posolyte against a negolyte with a dilute hydroxide concentration. In order to avoid rapid pH drifting during cell operation, buffer salts are used on the mild pH side to increase the proton buffer capacity under working pH. With proton-coupled electrochemistry functioning as proton pumps, pH drifting can be recovered and the pH difference between the posolyte and the negolyte can be maintained. This strategy can also be applied to pH-decoupling electrodeposition batteries, due to their potential for *in-situ* pH recovery. We found water-related proton-coupled chemistry, if not introducing unwanted side reactions, to be ideal as a proton pump. In comparing *in-situ* and *ex-situ* pH recovery strategies and considering the relationship between cell capacity balance and pH balance, we found that proton-coupled electrochemistry can work together with BPM based proton pumps to stabilize both the cell capacity balance and pH. Despite limitations associated with the stability, dendrite formation, metal ion crossover, buffer molecule interference, slow kinetics, or unwanted side reactions of most redox couples examined in this study, the concept of single membrane pH-decoupling with engineering of acid-base crossover and pH recovery can greatly broaden the scope for development of electrolyte chemistry and guide future works looking into pH-decoupling ARFBs in greater depth.

Supporting Information

Supporting Information is available from the online library or from the author.

Acknowledgements

This research was supported by U.S. DOE award DE-AC05-76RL01830 through PNNL subcontract 654799 and by the Harvard Climate Solution Change Fund. A.M.A acknowledges the MSE department at KFUPM and the Ministry of Education of Saudi Arabia for doctoral scholarship. The authors thank James MacArthur from Harvard Electronic Instrument Design Lab for developing multi-channel pH sensors.

Author Contributions

D.X., Z.Y., and A.M.A. designed and conducted cell tests and electrochemical experiments. D.X. conceived the idea. M.J.A. supervised the project. All authors drafted and edited the manuscript.

Conflict of Interest

View Article Online
DOI: 10.1039/D4YA00279B

The authors declare no conflict of interest.

Keywords

energy storage, pH-decoupling, high voltage, redox flow batteries, pH-recovery, proton-couple electron transfer

1. B. Dunn, H. Kamath and J.-M. Tarascon, *Science*, 2011, **334**, 928-935.
2. Y. Liang and Y. Yao, *Nat. Rev. Mater.*, 2022, **8**, 109-122.
3. Y. Yao, J. Lei, Y. Shi, F. Ai and Y.-C. Lu, *Nat. Energy*, 2021, **6**, 582-588.
4. R. Dmello, J. D. Milshtein, F. R. Brushett and K. C. Smith, *J. Power Sources*, 2016, **330**, 261-272.
5. L. Zhang, R. Feng, W. Wang and G. Yu, *Nat. Rev. Chem.*, 2022, **6**, 524-543.
6. D. G. Kwabi, Y. Ji and M. J. Aziz, *Chem. Rev.*, 2020, **120**, 6467-6489.
7. S. Muench, A. Wild, C. Friebe, B. Haupler, T. Janoschka and U. S. Schubert, *Chem. Rev.*, 2016, **116**, 9438-9484.
8. M. Park, J. Ryu, W. Wang and J. Cho, *Nat. Rev. Mater.*, 2016, **2**.
9. R. M. Darling, K. G. Gallagher, J. A. Kowalski, S. Ha and F. R. Brushett, *Energy Environ. Sci.*, 2014, **7**, 3459-3477.
10. M. L. Perry, K. E. Rodby and F. R. Brushett, *ACS Energy Lett.*, 2022, **7**, 659-667.
11. Y.-h. Zhu, Y.-f. Cui, Z.-l. Xie, Z.-b. Zhuang, G. Huang and X.-b. Zhang, *Nat. Rev. Chem.*, 2022, **6**, 505-517.
12. C. Lin, S.-H. Kim, Q. Xu, D.-H. Kim, G. Ali, S. S. Shinde, S. Yang, Y. Yang, X. Li, Z. Jiang and J.-H. Lee, *Matter*, 2021, **4**, 1287-1304.
13. Z. Yan, R. J. Wycisk, A. S. Metlay, L. Xiao, Y. Yoon, P. N. Pintauro and T. E. Mallouk, *ACS Cent Sci*, 2021, **7**, 1028-1035.
14. G.-M. Weng, C.-Y. V. Li and K.-Y. Chan, *J. Electrochem. Soc.*, 2013, **160**, A1384.
15. S. Gu, K. Gong, E. Z. Yan and Y. Yan, *Energy Environ. Sci.*, 2014, **7**, 2986-2998.
16. K. Gong, X. Ma, K. M. Conforti, K. J. Kuttler, J. B. Grunewald, K. L. Yeager, M. Z. Bazant, S. Gu and Y. Yan, *Energy Environ. Sci.*, 2015, **8**, 2941-2945.
17. A. S. Metlay, B. Chyi, Y. Yoon, R. J. Wycisk, P. N. Pintauro and T. E. Mallouk, *ACS Energy Lett.*, 2022, **7**, 908-913.
18. M. Park, E. S. Beh, E. M. Fell, Y. Jing, E. F. Kerr, D. Porcellinis, M. A. Goulet, J. Ryu, A. A. Wong, R. G. Gordon, J. Cho and M. J. Aziz, *Adv. Energy Mater.*, 2019, **9**.
19. D. Xi, A. M. Alfaraidi, J. Gao, T. Cochard, L. C. I. Faria, Z. Yang, T. Y. George, T. Wang, R. G. Gordon, R. Y. Liu and M. J. Aziz, *Nat. Energy*, 2024, DOI: 10.1038/s41560-024-01474-1.
20. F. Yu, L. Pang, X. Wang, E. R. Waclawik, F. Wang, K. K. Ostrikov and H. Wang, *Energy Storage Materials*, 2019, **19**, 56-61.
21. J. Lei, Y. Yao, Y. Huang and Y.-C. Lu, *ACS Energy Lett.*, 2022, **8**, 429-435.
22. C. Li, W. Wu, P. Wang, W. Zhou, J. Wang, Y. Chen, L. Fu, Y. Zhu, Y. Wu and W. Huang, *Adv. Sci*, 2019, **6**, 1801665.
23. X. Yuan, X. Wu, X. X. Zeng, F. Wang, J. Wang, Y. Zhu, L. Fu, Y. Wu and X. Duan, *Adv. Energy Mater.*, 2020, **10**, 2001583.

View Article Online
DOI: 10.1039/D4YA00279B

24. M. Mousavi, H. Dou, H. Fathiannasab, C. J. Silva, A. Yu and Z. Chen, *Chem. Eng. J.*, 2021, **412**, 128499.
25. J. Zhang, G. Jiang, P. Xu, A. G. Kashkooli, M. Mousavi, A. Yu and Z. Chen, *Energy Environ. Sci.*, 2018, **11**, 2010-2015.
26. J. Gao, K. Amini, T. Y. George, Y. Jing, T. Tsukamoto, D. Xi, R. G. Gordon and M. J. Aziz, *Adv. Energy Mater.*, 2022, **12**.
27. Y. Zhu, Y. Li, Y. Qian, L. Zhang, J. Ye, X. Zhang and Y. Zhao, *J. Power Sources*, 2021, **501**.
28. T. Kong, J. Liu, X. Zhou, J. Xu, Y. Xie, J. Chen, X. Li and Y. Wang, *Angew. Chem. Int. Ed.*, 2023, **62**, e202214819.
29. A. T. Murray, S. Voskian, M. Schreier, T. A. Hatton and Y. Surendranath, *Joule*, 2019, **3**, 2942-2954.
30. Y. Ji, M. A. Goulet, D. A. Pollack, D. G. Kwabi, S. Jin, D. Porcellinis, E. F. Kerr, R. G. Gordon and M. J. Aziz, *Adv. Energy Mater.*, 2019, **9**.
31. B. H. Robb, J. M. Farrell and M. P. Marshak, *Joule*, 2019, **3**, 2503-2512.
32. I. A. Digdaya, I. Sullivan, M. Lin, L. Han, W.-H. Cheng, H. A. Atwater and C. Xiang, *Nat. Commun.*, 2020, **11**, 4412.
33. J. Lei, Y. Zhang, Y. Yao, Y. Shi, K. L. Leung, J. Fan and Y.-C. Lu, *Nat. Energy*, 2023, DOI: 10.1038/s41560-023-01370-0, 1-10.
34. C. Zhong, B. Liu, J. Ding, X. Liu, Y. Zhong, Y. Li, C. Sun, X. Han, Y. Deng, N. Zhao and W. Hu, *Nat. Energy*, 2020, **5**, 440-449.
35. R. Thamizhselvan, R. Naresh, M. Ulaganathan, V. G. Pol and P. Ragupathy, *Electrochim. Acta*, 2023, **441**, 141799.
36. D. Zhao, Z. Zhuang, X. Cao, C. Zhang, Q. Peng, C. Chen and Y. Li, *Chem. Soc. Rev.*, 2020, **49**, 2215-2264.
37. S. E. Waters, B. H. Robb, S. J. Scappaticci, J. D. Saraidaridis and M. P. Marshak, *Inorg. Chem.*, 2022, **61**, 8752-8759.

Electronic Supplementary Material (ESI) for Energy Advances.

Supporting Information

Single-membrane pH-decoupling Aqueous Battery Using Proton-coupled Electrochemistry for pH Recovery

Dawei Xi[1], Zheng Yang[1], Abdulrahman M. Alfaraidi[1], Yan Jing[2], Roy G. Gordon[1,2], Michael J. Aziz[1,*]

1 John A. Paulson School of Engineering and Applied Sciences, Harvard University, Cambridge, MA, USA.

2 Department of Chemistry and Chemical Biology, Harvard University, Cambridge, MA, USA

Materials and methods

Materials and Synthesis

4,4′-bis(hydroxymethyl)-2,2′-bipyridine (Bhmbpy), manganese (II) acetate, acetic acid (HOAc), sodium acetate (NaOAc), Poly (acrylic acid) sodium salt (NaPAA, average MW 2000), NaCl, NaBr, NaOH, $ZnBr_2$, $FeCl_2$ were purchased from VWR International. (((9,10-dioxo-9,10-dihydroanthracene-2,6-diyl)bis(oxy))bis(propane-3,1-diyl))bis(phosphonic acid) (2,6-DPPEAQ) was purchased directly from TCI Chemicals. Fumasep® E-620K and Nafion® 212 as cation exchange membrane, and Selemion® DSV-N anion exchange membrane were purchased and only soaked in 1M NaCl or KCl solution before usage. 5 mg cm^{-2} Pt gas diffusion electrode (GDE) was purchased from fuel cell store.

1,4-BTMAPAQ was synthesized by mixing 40 mmol of dihydroxyanthraquinone, 88 mmol of anhydrous K_2CO_3, and 9.5 mmol of KI in 160 mL of anhydrous DMF. After stirring for 10 min, 88 mmol of 3-bromopropyl trimethylammonium bromide was introduced. The resulting dark mixture was sealed to exclude moisture and then stirred vigorously at 100 ˚C for 16 hours. 150 mL of ethyl acetate was added to the slurry after cooling, and then filtered to isolate a brown solid. The solid was dissolved in methanol, filtered to remove most of the inorganic salts. Filtrate was collected and evaporated until dry. The product was then dissolved in water and used an anion-exchange resin column to exchange bromide ions into chloride ions. This red solid was then dissolved in methanol to form a saturated solution, which was gradually added to 200 mL of ethyl acetate. Precipitates were collected by filtration to obtain the orange product.

$Fe(Bhmbpy)_3$ electrolyte was prepared by dissolving $FeCl_2$ (0.1 M) and Bhmbpy (0.35 M) with a ratio of 1:3.5 in 1 M NaCl, using HCl adjusting pH to 3. BTMAPAQ electrolyte was prepared by dissolving 1,4-BTMAPAQ (0.1 M) in 1 M NaCl, using NaOH adjusting pH to 12, if not claimed otherwise.

DPPEAQ electrolyte was prepared by dissolving 2,6-DPPEAQ (0.25 M) in 0.5 M NaCl, using NaOH adjusting pH to 12. NaBr electrolyte was prepared by dissolving NaBr (1 M) in water, then adding NaPAA (0.5 M sodium), adding 0.25 M HBr and 0.1 M Br_2.

$Mn(OAc)_2$ electrolyte was prepared by dissolving 1 M $Mn(OAc)_2$ in 3 M HOAc, adding 1 M NaOAc, 0.05 M KI. $Na_2Zn(OH)_4$ electrolyte was prepared by dissolving 1 M $Zn(OH)_2$ in 4 M NaOH.

Electrodes for flow battery cell tests were carbon papers (SGL 39AA) baked at 400 °C overnight. Electrodes for electrodeposition battery tests were 1 mm thick carbon cloths.

Cell cycling

Cycling of $Fe(Bhmbpy)_3$/BTMAPAQ cell was conducted in a 5 cm^2 flow battery, using 5 mL 0.1 M $Fe(Bhmbpy)_3$ as capacity limiting side, pairing with 10 mL 0.1 M negolyte. Electrolyte compositions are described in Materials and Synthesis without further treatment before usage. Electrolytes were pumped using a flow rate of 60 mL/min through 3 layers of baked carbon papers as electrodes. A Selemion DSV-N was used as the AEM. pH sensors were inserted in posolyte and negolyte. pH reading out was collected by an Arduino during cell operation and manually calibrated after. The cell was operated with a constant current (40 mA cm^{-2}) followed by constant potentials of 1.75 V (charging) and 0.4 V (discharging). During charging, the potential was held until the current density dropped lower than 5 mA cm^{-2}. During discharge, the current density cutoff was 1 mA cm^{-2} to ensure full discharge of the iron complex and its dimers. During operation, we would bubble air through the negolyte if the cell was out of balance.

Cycling of DPPEAQ/NaBr cell used 5 mL DPPEAQ electrolyte and 10 mL NaBr and Nafion 212 as the CEM, with other conditions the same as the $Fe(Bhmbpy)_3$/BTMAPAQ cell. Cut-off voltage was set as 2 V and 0.7 V with cut-off current density of 10 mA cm^{-2} and 5 mA cm^{-2}, for charge and discharge respectively.

Cell polarization

The full accessed capacity of the cell was first determined by performing a full charge/discharge cycling, which was accomplished by applying constant current followed by potential holds until the current decreased to the cutoff value. For semi-solid ARFBs, accessible capacity (100 SOC) was presumed to be 10 mAh cm^{-2}. The cell was then charged with intervals to various states of charge (calculated from the percentage of the total accessed capacity). To determine the high-frequency area-specific resistance (ASR), electrochemical impedance spectroscopy (EIS) measurements were conducted at each SOC with a perturbation of 10 mV and frequencies ranging from 1 to 100,000 Hz. The battery's open-circuit voltage (OCV) was also measured. Additionally, the potential was swept at each SOC at a scan rate of 100 mV s^{-1}, and the current response as a result was measured to create polarization curves. The polarization ASR was computed using the linear region of the polarization curves near OCV.

For galvanostatic tests, constant current densities between 20 to 80 mA cm^{-2} were applied during both charge and discharge cycles. Only $Fe(Bhmbpy)_3$/BTMAPAQ cell used potential holds during discharge. Consequently, the Coulombic, capacity utilization and energy efficiencies are calculated for each current density.

Supplementary notes

Supplementary Note. 1: Crossover of acid-base in a single-membrane pH-decoupling ARFB[1]

Crossover flux can be expressed by **Equation S1**. $[H^+]_p$, $[H^+]_n$ represent the proton concentrations in posolyte and negolyte, respectively. $[OH^-]_p$, $[OH^-]_n$ represent the hydroxide concentrations in posolyte and negolyte, respectively. l_{AEM} represents the thickness of AEM. j represents the signed ionic current, with direction pointing from posolyte to negolyte as positive. P represents the permeability coefficient of ions though the membrane. M represents the ion-migration coefficient inside the membrane due to the applied electric field. Specifically, the ion migration coefficients can be expressed as **Equation S2 – S3**. Here, D represents the diffusivity of an ion in a membrane. Z is the signed charge number of the ion. F is Faraday's constant. R is the universal gas constant and T is the absolute temperature. σ is the conductivity of the membrane in the electrolyte.

$$J_{crossover} = P_{H^+}^{AEM}\frac{[H^+]_p - [H^+]_n}{l_{AEM}} + M_{H^+}^{AEM} j + P_{OH^-}^{AEM}\frac{[OH^-]_n - [OH^-]_p}{l_{AEM}} + M_{OH^-}^{AEM} j \quad \text{(S1)}$$

$$M_{H^+}^{AEM} = D_{H^+}^{AEM}[H^+]_{AEM}\frac{ZF}{\sigma^{AEM}RT} \quad \text{(S2)}$$

$$M_{OH^-}^{AEM} = D_{OH^-}^{AEM}[OH^-]_{AEM}\frac{ZF}{\sigma^{AEM}RT} \quad \text{(S3)}$$

With a CEM setup, the crossover is described in **Equation S4 – S6**.

$$J_{crossover} = P_{OH^-}^{CEM}\frac{[OH^-]_n - [OH^-]_p}{l_{CEM}} + M_{OH^-}^{CEM} j + P_{H^+}^{CEM}\frac{[H^+]_p - [H^+]_n}{l_{CEM}} + M_{H^+}^{CEM} j \quad \text{(S4)}$$

$$M_{OH^-}^{CEM} = D_{OH^-}^{CEM}[OH^-]_{CEM}\frac{ZF}{\sigma^{CEM}RT} \quad \text{(S5)}$$

$$M_{H^+}^{CEM} = D_{H^+}^{CEM}[H^+]_{CEM}\frac{ZF}{\sigma^{CEM}RT} \quad \text{(S6)}$$

In these equations, crossover of protons through AEMs and hydroxide through CEMs have been described in our previous work. The crossover (exchange) of protons through CEMs and hydroxide through AEMs can be estimated as **Equation S7 – S12**. K_X^Y is the conductivity of Z charged ion X in membrane Y.

For protons through CEMs:

$$J_{protons,CEM} \approx M_{H^+}^{CEM} j \quad \text{(S7)}$$

$$M_{H^+}^{CEM} \approx \frac{[H^+]_p K_{H^+}^{CEM}}{[H^+]_p K_{H^+}^{CEM} + \sum z[other\ cations^{z+}]_p K_{other\ cations^{z+}}^{CEM}} \quad \text{(S8)}$$

For hydroxide through AEMs:

$$J_{hydroxides,AEM} \approx M_{OH^-}^{AEM} j \tag{S9}$$

$$M_{OH^-}^{AEM} \approx \frac{[OH^-]_n K_{OH^-}^{AEM}}{[OH^-]_n K_{OH^-}^{AEM} + \sum z[other\ anions^{z-}]_n K_{other\ anions^{z-}}^{AEM}} \tag{S10}$$

For protons through AEMs:

$$J_{protons,AEM} \approx P_{H^+}^{AEM} \frac{[H^+]_p - [H^+]_n}{l_{AEM}} \tag{S11}$$

For hydroxides through CEMs:

$$J_{hydroxides,CEM} \approx P_{OH^-}^{CEM} \frac{[OH^-]_n - [OH^-]_p}{l_{CEM}} \tag{S12}$$

For example, in the case of Fe(Bhmbpy)$_3$/BTMAPAQ cell, the acid crossover flux from pH 2 – 4 buffer solution was extracted from reported data,[1] determined to be lower than 1 nmol s^{-1} cm^{-2}. The hydroxide crossover flux from pH 12 solution was estimated using equation S11, because the conductivity of hydroxide and chloride anions are similar in Selemion DSV-N:

$$J_{hydroxides,AEM} \approx M_{OH^-}^{AEM} j \ _{=} \frac{0.01\ M}{0.01M + 1M} * 40mA\ cm^{-2} \approx 4\ nmol\ s^{-1} cm^{-2} \tag{S11}$$

The number of moles of the acid-base crossover can be calculated as:

$n_{net\ crossover} = AtJ_{crossover}$

A is the membrane area, t is the charging/discharging duration.

The changing of acid/base concentration can be calculated as:

$c_{net\ crossover} = n_{net\ crossover}/V$

V is the volume of electrolyte. With a fixed charging/discharging current density, t/V is unchanged when only changing the volume of electrolyte. Therefore, the influence of acid-base crossover is decoupled from the electrolyte volume (total capacity).

Supplementary Note. 2: OER as proton sources for bromide posolyte

Oxygen evolution reaction (OER) requires a high potential (thermodynamically 1.23 V vs. RHE, with high overpotential of hundreds of millivolts), posing risk of over-oxidizing molecules. For example, iodine can be oxidized during OER:

$0.5I_2 + 3H_2O - 5e^- \rightarrow 6H^+ + IO_3^-$ ϕ = 1.2 V vs. SHE, pH 0

Bhmbpy can be oxidized during OER or by oxidants[2]:

Bhmbpy + $H_2O - 2e^- \rightarrow 2H^+$ + Bhmpby-O

Owing to the high voltage of BrO_3^-/Br_2, with appropriate OER catalysts, OER can happen without driving unfavored irreversible oxidation of bromine:

$3Br^- - 2e^- \rightarrow Br_3^-$ ϕ = 1.09 V vs. SHE, pH 0

$0.5Br_2 + 3H_2O - 5e^- \rightarrow 6H^+ + BrO_3^-$ ϕ = 1.5 V vs. SHE, pH 0

$H_2O - 2e^- \rightarrow 2H^+ + 0.5\ O_2$ ϕ = 1.23 V vs. SHE, pH 0

But anti-oxidation electrodes and buffers are required to avoid oxidation side reactions. PAA and acetate can be oxidized by bromine. Inorganic buffers like phosphate can be an alternative.

Supplementary Note. 3: BPM sub-cell for pH recovery in pH-decoupling electrodeposition batteries

Using the BPM sub-cell for pH-recovery has many benefits. Because electrolytes are discharged in the sub-cell, working voltage of the BPM cell will not post extra risks toward electrolyte decomposition. However, pumping electrolytes into the sub-cell for ex-situ pH recovery has an intrinsic requirement that both the oxidized and reduced form of the redox active molecule have to be soluble and flowable. This makes the sub-cell hard to be used in pH-decoupling electrodeposition batteries. For example, Zn and MnO_2 can hardly be pumped out into BPM cell to be discharged. Flowable redox mediators are required, in order to use BPM sub-cell for pH recovery in pH-decoupling electrodeposition batteries.

The solution to this problem is to introduce a low concentration of flowable redox couple. Flowable redox couples are actually already added in many electrodeposition batteries to increase the kinetics and reversibility of the cells. For example, people have developed using iodine for MnO_2 posolyte and flavin mononucleotide for polysulfide negolyte.

The same molecule can be added into both posolyte and negolyte, as long as it fits the requirements. The requirements of the adding flowable redox molecules are: 1. Low concentration. It cannot be the main redox couple that controls the charging and discharging of the cell. 2. Reversibility. The charging and discharging of the added molecules better not require large overpotential. 3. Compatible with the main redox couple. It cannot accelerate or cause decomposition of the original electrolyte. 4. Stability. The fade rate of itself should not be too high (> 0.1 %/day). 5. Suitable redox potential. This is the most important requirement. The potential of the added flowable redox molecules requires to be lower than the posolyte, but higher than the negolyte. In which case, during charging, the added molecules will become oxidized form in the posolyte and reduced form in the negolyte before charging of the main couples happen. Also, they will remain oxidized in the posolyte and reduced in the negolyte during cell cycling, because the cell does not have to hit the discharge voltage of the added couple. They can be discharged in the BPM sub-cell,

generating acid and base, and be oxidized/reduced back by chemical or electrochemical reactions in the main cell, mediating the acid-base generation by mediating the charge transfer from the main cell into sub-cell.

Supplementary Table

Supplementary Table S1: Redox molecule candidates**.**

Name & Structure	Voltage (V vs. SHE)	Working pH	Note	Reference
Ce_2O^{6+}/Ce^{3+}	1.81	< 0	Posolyte. Cation. Strong acid, need to consider acid crossover. Need to check water splitting.	[3]
Ce^{4+}/Ce^{3+}	1.44	< 0	Posolyte. Cation. Strong acid, need to consider acid crossover. Voltage changes with anions. Need to check water splitting.	[4]
Cl_2/Cl^-	1.36	< 7	Posolyte. Anion. High vapor pressure.	
MnO_2/Mn^{2+}	1.22 (pH = 0)	< 2	Posolyte. Cation. Strong acid, need to consider acid crossover. Proton coupled.	[5]
Br_3^-/Br^-	1.09	< 7	Posolyte. Anion. High vapor pressure.	[6]
VO_2^+/VO^{2+}	1.04 (pH = 0)	< 1	Posolyte. Cation. Strong acid, need to consider acid crossover. Proton coupled.	[7]
TEMPTMA 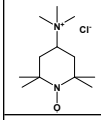	0.60	~ 7	Posolyte. Cation.	[8]
TEMPO-4-sulfate 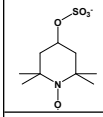	0.86	~7	Posolyte. Anion.	[9]
$Fe^{3+/2+}(Bhmbpy)_3$ Bhmbpy: 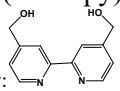	0.98	2 – 4	Posolyte. Cation.	[2]
$Na_4[Fe^{3+/2+}(Dcbpy)_2(CN)_2]$ Dcbpy: 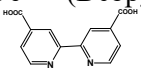	0.64	3 – 12	Posolyte. Anion.	[10]
$MnO_2/Mn(OAc)_2$	0.85	4	Posolyte. Cation.	[11]
TMAP-TEMPO	0.80	~ 7	Posolyte. Cation.	[12]

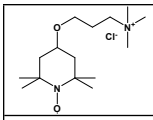				
4-OH-TEMPO 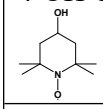	0.81	~ 7	Posolyte. Cation.	[13]
Fe^{3+}/Fe^{2+}	0.77	< 3	Posolyte. Cation.	[14]
FcNCl ($Fe^{3+/2+}$) 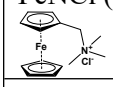	0.61	~ 7	Posolyte. Cation.	
Fc-SO_3Na 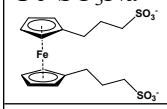	0.3	~ 7	Posolyte. Anion.	[15]
I_3^-/I^-	0.54	< 7	Posolyte. Anion.	[16]
Fc⊂β-CD ($Fe^{3+/2+}$) 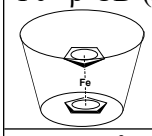	0.5	~ 7	Posolyte. Cation.	[17]
$Fe(CN)_6^{3-}$/ $Fe(CN)_6^{4-}$	0.4	> 7	Posolyte. Anion.	
BTMAP-Fc ($Fe^{3+/2+}$) 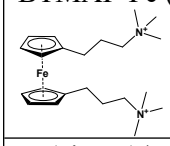	0.39	~ 7	Posolyte. Cation.	[18]
Fe(citrate)/ Fe(citrate)$^-$	0	~ 3.5	Anion.	[19]
S_4^{2-}/S_2^{2-}	−0.42	> 11	Negolyte. Anion.	[20]
BPP-Vi 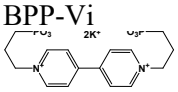	−0.46	~ 7	Negolyte. Anion.	[21]
2,6-DBEAQ 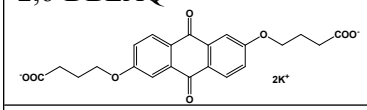	−0.52 (pH 12)	> 12	Negolyte. Anion.	[22]
2,6-DPPEAQ 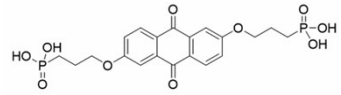	−0.50 (pH 12)	> 7	Negolyte. Anion.	[23]
DHAQ 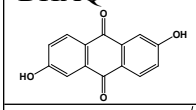	−0.68 (pH 14)	14	Negolyte. Anion.	[24]
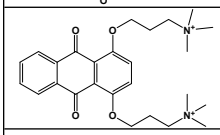	−0.55 (pH 12)	> 7	Negolyte. Cation. Proton coupled when pH < 12.	[9]
BHPC 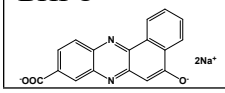	−0.78 (pH 14)	> 12	Negolyte. Anion. Proton coupled.	[25]

DHPS 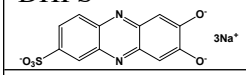	−1.05 (pH 14)	> 13	Negolyte. Anion. Proton coupled.	[26]
1,8-PFP 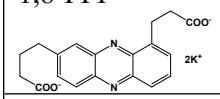	−0.57 (pH 14)	> 7	Negolyte. Anion. Proton coupled.	[27]
7,8-hydroxyalloxazine 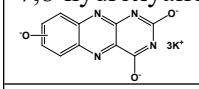	−0.72 (pH 14)	14	Negolyte. Anion. Proton coupled.	[28]
$Fe^{3+/2+}$(TEOA) 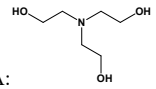 TEOA:	−0.78	13	Negolyte. Anion.	[19]
Methyl viologen 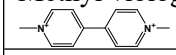	−0.42	~ 7	Negolyte. Cation.	[13]
BTMAP-Vi 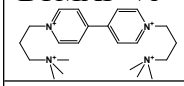	−0.40	~ 7	Negolyte. Cation.	[18]
Diquat 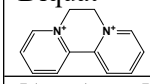	−0.37	~ 7	Negolyte. Cation.	[29]
$[(NPr)_2PV]$-4Cl 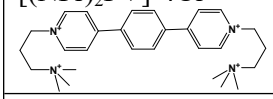	−0.78	~ 7	Negolyte. Cation.	[30]
$Fe^{3+/2+}$(DIPSO) 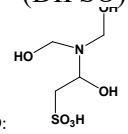 DIPSO:	−0.82	> 13	Negolyte. Anion.	[31]
$Cr^{3+/2+}$ (PDTA) 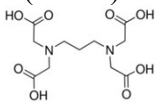 PDTA:	−1.18	~ 9	Negolyte. Anion. Need to check water splitting.	[32]
$Zn/Zn(OH)_4^{2-}$	−1.22 (pH 14)	> 14	Negolyte. Anion. Strong base. Need to consider base crossover. Need to check water splitting.	[33]

Supplementary Table S2: Potential proton pumps**.** Any oxidation half-reaction may be paired with any reduction half-reaction. The last entry is a full reaction.

Reaction	Potential, V vs. RHE	Type	Note
Hydrogen evolution reaction (HER)	0	Reduction, hydroxide	Catalysts are not necessary. Be cautious of over-reduction of molecules. Some redox

$2H_2O + 2e^- \rightarrow H_2 + 2OH^-$		source	couples have this side reaction occurring spontaneously.[4,32]
Hydrogen oxidation reaction (HOR) $H_2 - 2e^- \rightarrow 2H^+$	0	Oxidation, proton source	Catalysts and hydrogen gas are required. Be cautious of decomposition of molecules on HOR catalysts. Usually *ex-situ*.
Oxygen evolution reaction (OER) $2H_2O - 4e^- \rightarrow O_2 + 2H^+$	1.23	Oxidation, proton source	Catalysts may be required because of bad kinetics. Be cautious of oxidation of carbon electrodes and molecules. Some redox couples have this side reaction occurring spontaneously.[34]
Oxygen reduction reaction (ORR, 2e) $H_2O + O_2 + 2e^- \rightarrow HO_2^- + OH^-$ (pKa of H_2O_2 is about 11.7)	0.68 (pH < 12)	Reduction, hydroxide source	Usually spontaneous when introducing air into the negolyte. The amount of air introduced should be controlled.
Oxygen reduction reaction (ORR, 4e) $2H_2O + O_2 + 4e^- \rightarrow 4OH^-$	1.23	Reduction, hydroxide source	Usually spontaneous when introducing air into the negolyte. The amount of air introduced should be controlled.
BPM: $H_2O \rightarrow H^+$ (pH 0) + OH^- (pH 14)	0.83 V, full cell	Water dissociation, source of protons and hydroxide	Must be *ex-situ* in a sub-cell. Flowable mediators must be introduced when working on electrodeposition batteries. Driven by discharging of the electrolytes.

Supplementary figures

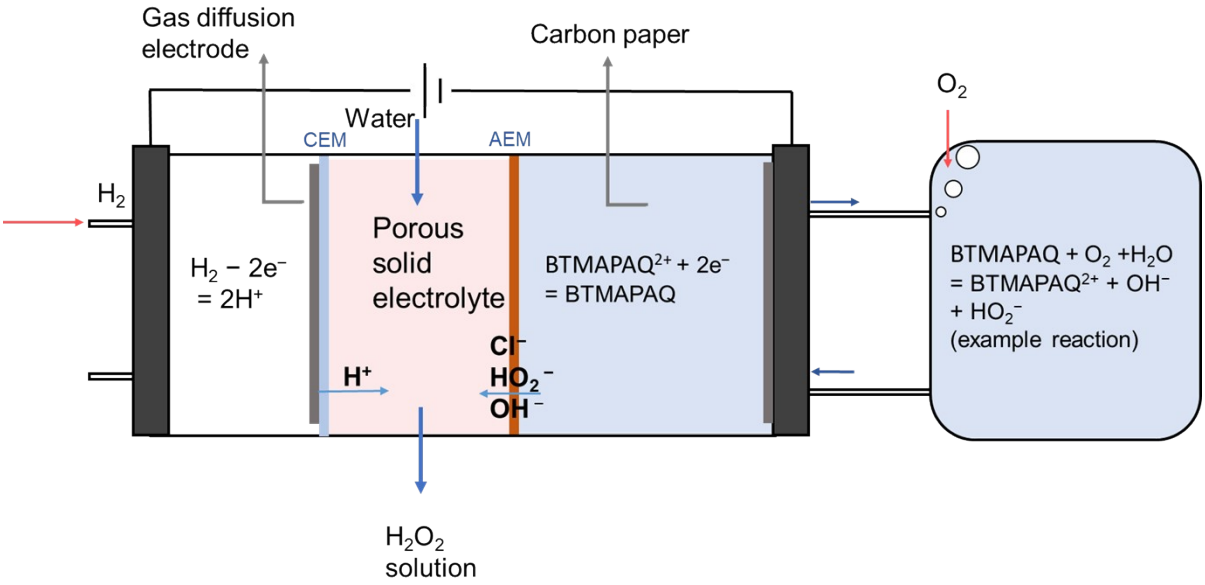

Supplementary Fig. S1 | Cell structure of H_2O_2 production using BTMAPAQ mediated ORR. The formation of H_2O_2 in the center chamber suggests the formation and electromigration of HO_2^-.

The support the generation and migration of HO_2^-, we assembled a three-chamber, two-membrane electrochemical cell,[35] as shown in **Supplementary Fig. S1**. The cell was operated under a constant current of 20 mA cm^{-2}. Air was continuously bubbled through the BTMAPAQ catholyte (0.2 M, 5 mL). With this setup, we collected the solution exiting the center chamber and detected the formation of H_2O_2. We used $KMnO_4$ to titrate the solution to determine the molarity of the generated hydrogen peroxide. The Faradaic efficiency (FE) of the 2e ORR reaction was calculated using the following equation, where n_{H2O2} stands for the molarity of the obtained H_2O_2. F is the Faradaic constant. Q is the charge passing through the circuit.

$$FE = n_{H2O2} * 2 * F/Q$$

The Faradaic efficiency was about 3% – 8% when the system reached a steady state, which we interpret as the formation and electromigration of HO_2^- through the AEM.

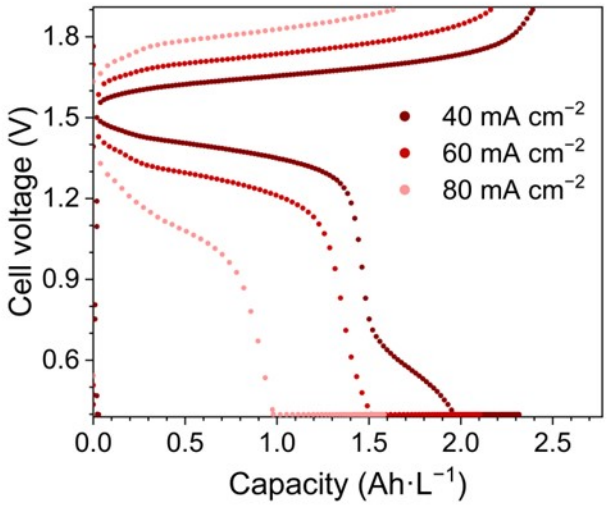

Supplementary Fig. S2 | Galvanostatic tests for the Fe(Bhmbpy)$_3$/BTMAPAQ cell at 40, 60 and 80 mA cm^{-2}. Theoretical capacity is about 2.77 Ah L^{-1}. Cutoff voltage is 1.9 V, and 0.4 V for charging and discharging. Voltage hold was applied during discharge until current dropping lower than 1 mA cm^{-2}. Dimerization and ligand self-oxidation of Fe(Bhmbpy)$_3$ make the cell hardly practicable.

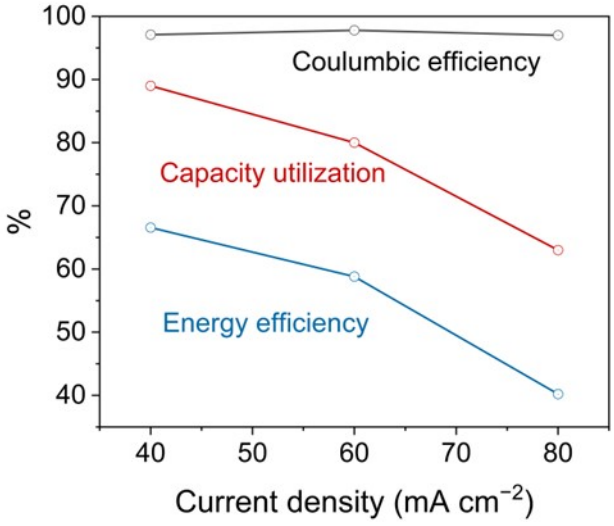

Supplementary Fig. S3 | Capacity utilization and Coulombic and round-trip energy efficiencies vs. applied current density for the Fe(Bhmbpy)$_3$/BTMAPAQ cell during galvanostatic tests.

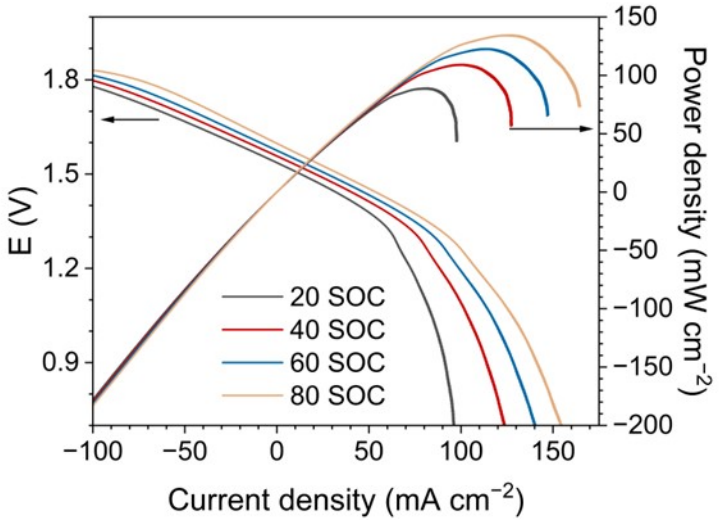

Supplementary Fig. S4 | Cell voltage and power density during discharge of the Fe(Bhmbpy)$_3$/BTMAPAQ cell at different states of charge. Power density is not high mainly due to the mass transport limitation.

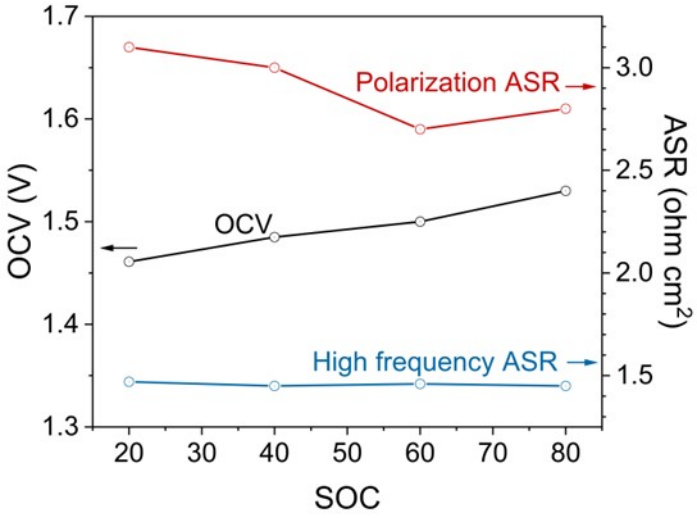

Supplementary Fig. S5 | Dependence on SOC of OCV and ASR near OCV for the Fe(Bhmbpy)$_3$/BTMAPAQ cell. Ohmic resistance and charge transfer resistance can also be further engineered for a higher power.

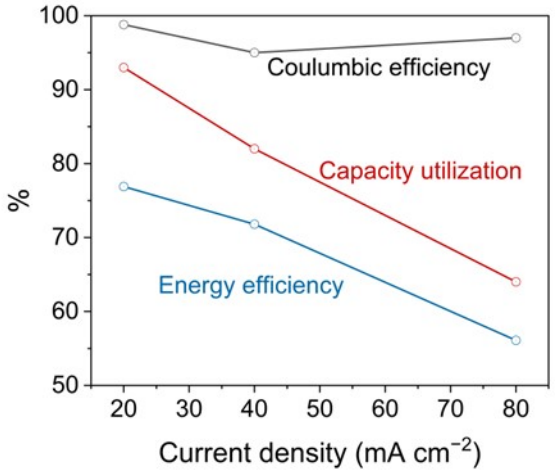

Supplementary Fig. S6 | Capacity utilization and Coulombic and round-trip energy efficiencies vs. applied current density for the NaBr/DPPEAQ cell during galvanostatic tests. Bromine and crossover of bromine oxidizes the membrane, electrode, buffer and DPPEAQ making the cell hardly practicable.

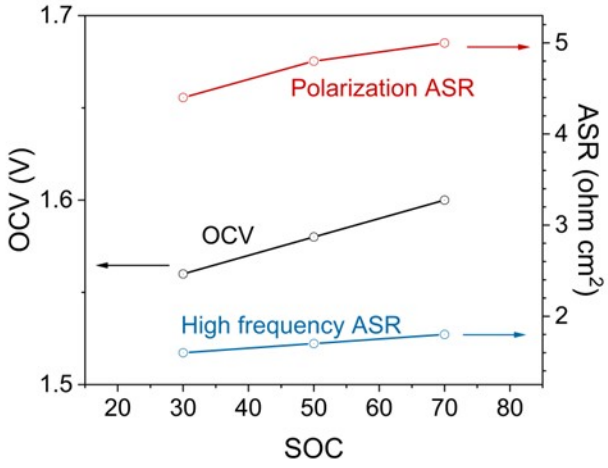

Supplementary Fig. S7 | Dependence on SOC of OCV and ASR near OCV for the NaBr/DPPEAQ cell.

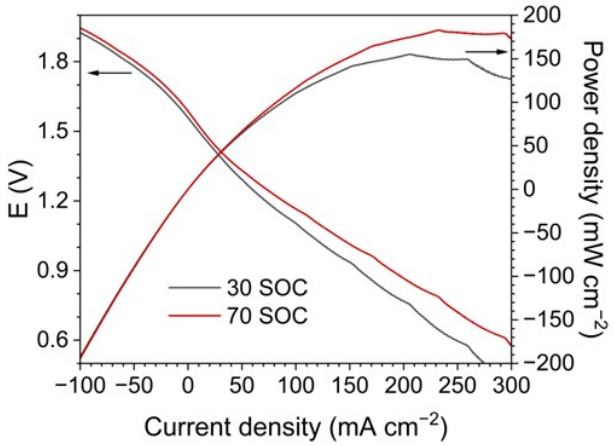

Supplementary Fig. S8 | Cell voltage and power density during discharge of the NaBr/DPPEAQ cell at different states of charge. Power density is not high mainly due to high ohmic resistance of the cell and slow kinetic of NaBr-$NaBr_3$ couple.

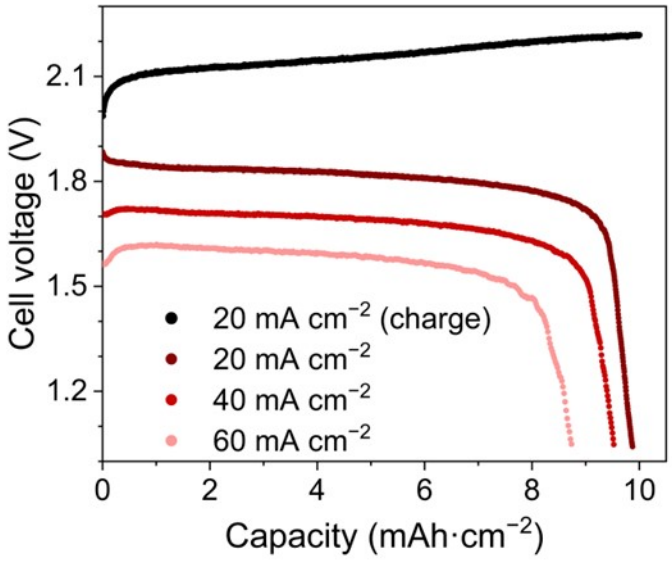

Supplementary Fig. S9 | Galvanostatic tests for the $Mn(OAc)_2/Na_2Zn(OH)_4$ cell at 20, 40, 60 and 80 mA cm^{-2}. Charging capacity is set as 10 mAh cm^{-2}. Cutoff voltage is 1.0 V for discharging. Crossover of Mn ions, Zn ions, dendrites formation and oxidation of acetates when applying OER for pH recovery making the cell hardly practicable.

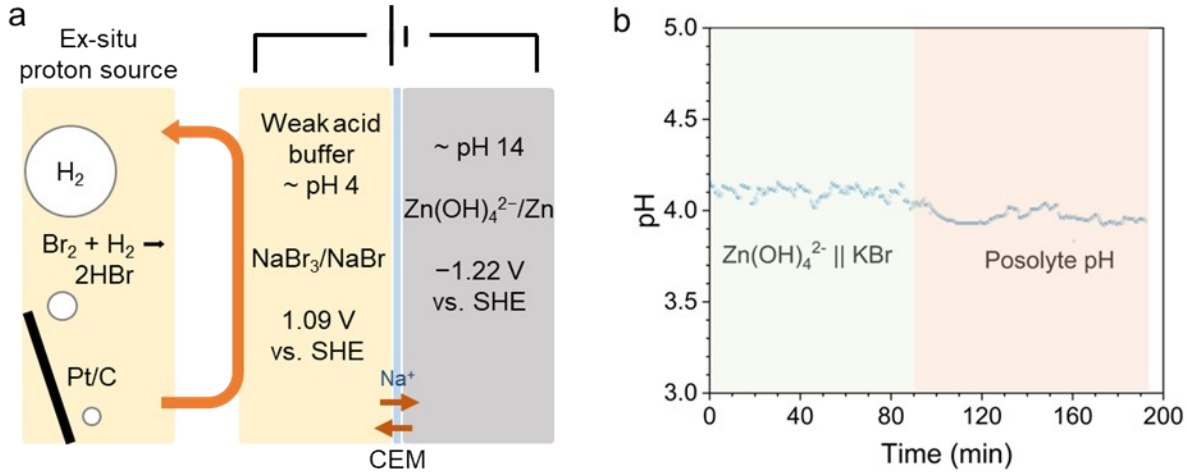

Supplementary Fig. S10 | Hydrogen oxidation as proton generator. a, A schematic of the system. Bromine was used as the flowable posolyte. HOR was catalyzed by a commercial Pt GDE. **b,** pH of the posolyte bromine/bromide side (green shaded) after introducing hydrogen (red shaded). pH of the buffered posolyte went lower due to the generation of protons.

References for Supplementary Information

1. D. Xi, A. M. Alfaraidi, J. Gao, T. Cochard, L. C. I. Faria, Z. Yang, T. Y. George, T. Wang, R. G. Gordon, R. Y. Liu and M. J. Aziz, *Nat. Energy*, 2024, DOI: 10.1038/s41560-024-01474-1.
2. J. Gao, K. Amini, T. Y. George, Y. Jing, T. Tsukamoto, D. Xi, R. G. Gordon and M. J. Aziz, *Adv. Energy Mater.*, 2022, **12**.
3. S. Gu, K. Gong, E. Z. Yan and Y. Yan, *Energy Environ. Sci.*, 2014, **7**, 2986-2998.
4. P. K. Leung, C. Ponce-de-León, C. T. J. Low, A. A. Shah and F. C. Walsh, *J. Power Sources*, 2011, **196**, 5174-5185.
5. C. Zhong, B. Liu, J. Ding, X. Liu, Y. Zhong, Y. Li, C. Sun, X. Han, Y. Deng, N. Zhao and W. Hu, *Nat. Energy*, 2020, **5**, 440-449.
6. B. Huskinson, M. P. Marshak, C. Suh, S. Er, M. R. Gerhardt, C. J. Galvin, X. Chen, A. Aspuru-Guzik, R. G. Gordon and M. J. Aziz, *Nature*, 2014, **505**, 195-198.
7. G.-M. Weng, C.-Y. V. Li and K.-Y. Chan, *Materials Today Energy*, 2018, **10**, 126-131.
8. T. Janoschka, N. Martin, M. D. Hager and U. S. Schubert, *Angewandte Chemie International Edition*, 2016, **55**, 14427-14430.
9. J. Winsberg, C. Stolze, A. Schwenke, S. Muench, M. D. Hager and U. S. Schubert, *ACS Energy Lett.*, 2017, **2**, 411-416.
10. X. Li, P. Gao, Y.-Y. Lai, J. D. Bazak, A. Hollas, H.-Y. Lin, V. Murugesan, S. Zhang, C.-F. Cheng and W.-Y. Tung, *Nat. Energy*, 2021, **6**, 873-881.
11. J. Lei, Y. Yao, Y. Huang and Y.-C. Lu, *ACS Energy Lett.*, 2022, **8**, 429-435.
12. Y. Liu, M.-A. Goulet, L. Tong, Y. Liu, Y. Ji, L. Wu, R. G. Gordon, M. J. Aziz, Z. Yang and T. Xu, *Chem*, 2019, **5**, 1861-1870.
13. T. Liu, X. Wei, Z. Nie, V. Sprenkle and W. Wang, *Adv. Energy Mater.*, 2016, **6**, 1501449.
14. K. Gong, X. Ma, K. M. Conforti, K. J. Kuttler, J. B. Grunewald, K. L. Yeager, M. Z. Bazant, S. Gu and Y. Yan, *Energy Environ. Sci.*, 2015, **8**, 2941-2945.
15. J. Yu, M. Salla, H. Zhang, Y. Ji, F. Zhang, M. Zhou and Q. Wang, *Energy Storage Materials*, 2020, **29**, 216-222.
16. M. Mousavi, H. Dou, H. Fathiannasab, C. J. Silva, A. Yu and Z. Chen, *Chem. Eng. J.*, 2021, **412**, 128499.
17. Y. Li, Z. Xu, Y. Liu, S. Jin, E. M. Fell, B. Wang, R. G. Gordon, M. J. Aziz, Z. Yang and T. Xu, *ChemSusChem*, 2021, **14**, 745-752.
18. E. S. Beh, D. De Porcellinis, R. L. Gracia, K. T. Xia, R. G. Gordon and M. J. Aziz, *ACS Energy Lett.*, 2017, **2**, 639-644.
19. K. Gong, F. Xu, J. B. Grunewald, X. Ma, Y. Zhao, S. Gu and Y. Yan, *ACS Energy Lett.*, 2016, **1**, 89-93.
20. J. Lei, Y. Zhang, Y. Yao, Y. Shi, K. L. Leung, J. Fan and Y.-C. Lu, *Nat. Energy*, 2023, DOI: 10.1038/s41560-023-01370-0, 1-10.
21. S. Jin, E. M. Fell, L. Vina-Lopez, Y. Jing, P. W. Michalak, R. G. Gordon and M. J. Aziz, *Adv. Energy Mater.*, 2020, **10**.
22. D. G. Kwabi, K. Lin, Y. Ji, E. F. Kerr, M.-A. Goulet, D. De Porcellinis, D. P. Tabor, D. A. Pollack, A. Aspuru-Guzik, R. G. Gordon and M. J. Aziz, *Joule*, 2018, **2**, 1894-1906.
23. Y. Ji, M. A. Goulet, D. A. Pollack, D. G. Kwabi, S. Jin, D. Porcellinis, E. F. Kerr, R. G. Gordon and M. J. Aziz, *Adv. Energy Mater.*, 2019, **9**.
24. K. Lin, Q. Chen, M. R. Gerhardt, L. Tong, S. B. Kim, L. Eisenach, A. W. Valle, D. Hardee, R. G. Gordon and M. J. Aziz, *Science*, 2015, **349**, 1529-1532.

25. C. Wang, X. Li, B. Yu, Y. Wang, Z. Yang, H. Wang, H. Lin, J. Ma, G. Li and Z. Jin, *ACS Energy Lett.*, 2020, **5**, 411-417.
26. A. Hollas, X. Wei, V. Murugesan, Z. Nie, B. Li, D. Reed, J. Liu, V. Sprenkle and W. Wang, *Nat. Energy*, 2018, **3**, 508-514.
27. J. Xu, S. Pang, X. Wang, P. Wang and Y. Ji, *Joule*, 2021, **5**, 2437-2449.
28. K. Lin, R. Gómez-Bombarelli, E. S. Beh, L. Tong, Q. Chen, A. Valle, A. Aspuru-Guzik, M. J. Aziz and R. G. Gordon, *Nat. Energy*, 2016, **1**.
29. J. Huang, Z. Yang, V. Murugesan, E. Walter, A. Hollas, B. Pan, R. S. Assary, I. A. Shkrob, X. Wei and Z. Zhang, *ACS Energy Lett.*, 2018, **3**, 2533-2538.
30. M. Pan, Y. Lu, S. Lu, B. Yu, J. Wei, Y. Liu and Z. Jin, *ACS Appl. Mater. Interfaces*, 2021, **13**, 44174-44183.
31. M. Shin, C. Noh, Y. Chung and Y. Kwon, *Chem. Eng. J.*, 2020, **398**.
32. B. H. Robb, J. M. Farrell and M. P. Marshak, *Joule*, 2019, **3**, 2503-2512.
33. F. Yu, L. Pang, X. Wang, E. R. Waclawik, F. Wang, K. K. Ostrikov and H. Wang, *Energy Storage Materials*, 2019, **19**, 56-61.
34. T. Kong, J. Liu, X. Zhou, J. Xu, Y. Xie, J. Chen, X. Li and Y. Wang, *Angew. Chem. Int. Ed.*, 2023, **62**, e202214819.
35. C. Xia, Y. Xia, P. Zhu, L. Fan and H. Wang, *Science*, 2019, **366**, 226-231.